

Contents lists available at ScienceDirect

Journal of Sound and Vibration

journal homepage: www.elsevier.com/locate/jsvi



Discrete and periodic vortex loading on a flexible plate; application to energy harvesting and voiced speech production



Alireza Pirnia a, Emily A. Browning a, Sean D. Peterson b, Byron D. Erath a,*

- ^a Department of Mechanical and Aeronautical Engineering, Clarkson University, 8 Clarkson Ave., Box 5725, Potsdam, NY 13699, USA
- b Department of Mechanical and Mechatronics Engineering, University of Waterloo, 200 University Avenue West, Waterloo, Ontario N2L 3G1, Canada

ARTICLE INFO

Article history: Received 18 December 2017 Revised 21 May 2018 Accepted 30 May 2018 Available online 25 July 2018 Handling Editor: L. Huang

Keywords: Flow-induced vibration Vortex ring Energy harvesting Voiced speech

ABSTRACT

Flow-induced vibrations of flexible surfaces driven by coherent vortical structures are ubiquitous in engineering and biological flows; from the extraction of fluidic energy via oscillating electro-active polymers to vocal fold dynamics during voiced speech production. These scenarios may involve either discrete or periodic loading conditions due to the advection of vortices past the structure. This work considers, as a function of the vortex production frequency, the fluid-structure interaction that occurs as vortices are propagated tangentially over flexible plates with variable structural properties. Velocity fields are acquired with particle image velocimetry and used to compute the vorticity and pressure fields, while the plate energy is estimated from its kinematics. Primary and secondary peaks in plate deflection amplitude and the plate energy as a function of vortex production frequency are observed at integer fractions of the fundamental plate frequency. At resonance conditions, plate energy relative to discrete vortex loading is increased by approximately three orders of magnitude, while the sub-harmonics increase the plate energy by about two orders of magnitude. Additional physical influences on the energy exchange process, including vortex-to-plate spacing and Strouhal number, are also investigated, detailing the importance of spatial and temporal interactions. The magnitude of the initial plate deflection as the vortex ring approaches the plate, due to persistent vibrations from previous interactions, is shown to retard the time at which the maximum load is applied as the increased relative vortex-to-plate spacing weakens cross-sign vorticity interactions. Finally, plate properties are scaled to model the structural properties of the vocal folds and the effect of intra-glottal vortices on vocal fold dynamics is quantified, where a negligible influence is observed.

© 2018 Elsevier Ltd. All rights reserved.

1. Introduction

Flow-induced vibrations due to vortical structures have been a topic of interest for decades [1-3]. Vortex production within a flow field may arise for a variety of reasons, including flow separation [1], turbulent boundary layer formation [4], or in the wakes of bluff bodies [5]. If a flexible plate is immersed in a fluid flow, unsteady disturbances in the pressure field will incite vibrations in the structure. Variations in the fluid physics and plate properties can produce a wide range of structural responses [6], where vibrations induced by vortices may be employed to extract energy from the ambient environment by using electroactive polymers, which convert strain energy into electrical energy [7-10]. The extracted energy can be used to power both small and medium-scale devices such as consumer electronics [11], structural health monitors [7] and aquatic tracking systems

E-mail address: berath@clarkson.edu (B.D. Erath).

st Corresponding author.

[12]. In energy harvesting applications, flexible plates are often placed in the wake of a bluff body, where a von Kármán vortex street is formed, giving rise to vortices that periodically advect over both sides of the plate, inciting oscillations that can be converted to electrical energy [9,13–17].

Plate dynamics under periodic fluid loading have been investigated for a variety of scenarios in an attempt to increase plate oscillation amplitudes and the subsequent energy extraction. When placed in the wake of a bluff body, the maximum voltage output from piezoelectric plates has been shown to occur when the periodic vortex shedding frequency is matched with the natural frequency of the plate [18]. Higher plate oscillation modes have also been found to lock-on to the shedding frequency of the von Kármán vortex street that forms in the wake, where the amplitude of these modes is correlated with the width of the undisturbed vortex street [19]. Using PIV, it has also been shown that deformation of the membrane is synchronized with the position of the vortices passing over it. In all of these studies, plate oscillations were maximized by matching the vortex production frequency with the fundamental frequency of the plate. This condition is often used as a design criterion for energy harvesting applications; however, the conditions where the frequencies were not matched (off-design conditions) have not been considered.

While most coherent vortical structures, like those found in a von Kármán vortex street, provide cyclic loading, in the more general case, vortices may be generated randomly or at varying frequencies. To this end, some studies have considered the interaction of discrete vortices with deformable surfaces. Peterson and Porfiri [20] reported that approximately 1% of a vortex ring's energy will be transferred into plate strain energy when it normally impacts the tip of a plate. Numerical investigations of similar configurations utilizing a vortex dipole, as opposed to a vortex ring, have explored the influence of Reynolds number, finding a maximum of approximately 5% energy transfer from the vortex dipole to the plate is achievable [21], with recent experimental investigations validating the numerical findings [22].

Goushcha et al. [23] performed an experimental study of vortex rings advecting tangentially over a plate, for both discrete and periodic vortex production. This configuration is analogous to off-design energy harvesting conditions where a shift in flow trajectory may move a flexible structure outside of the wake of a leading bluff body. When two consecutive vortices with a period of vortex production equal to the fundamental period of plate oscillation advected over the plate the maximum deflection amplitude was increased. However, the steady-state plate response to continuous periodic vortex loading, and for varying vortex production frequencies, was not reported.

More recently, a fluid-structure interaction model of the same configuration as Goushcha et al. [23] was developed [24] by coupling a potential flow model with Kirchhoff-Love plate theory [25]. Differences between the numerical and experimental approaches were observed due to insufficient experimental data to fully-validate the numerical model and the inherent assumption of inviscid flow in the potential flow model. There is, therefore, still a lack of understanding regarding the steady-state response of cantilevered plates when subjected to periodic, unilateral loading that is not synchronized with the plate fundamental frequency, and a determination of how this impacts the fluid-plate energy exchange.

Periodic pressure loadings due to vortex advection over a flexible surface are also of interest in the study of voiced speech production [26–29]. Vortices are produced as the glottis (the opening between the vocal folds) forms into a divergent channel during the closing phases of the phonatory cycle, producing an adverse pressure gradient that leads to flow separation and vortex formation within the glottis [29]. Difficulties in definitively determining the impact of intra-glottal vortices on the vocal fold dynamics arise, however, due to the challenge in decoupling the vortex pressure loading from the total aerodynamic loading. Nevertheless, it has been hypothesized that these separation vortices have a significant impact on the vocal fold dynamics, with the reduced core pressure assisting in the rapid closure of the vocal folds, thereby enhancing the resultant acoustical energy content [28,30,31]. To the contrary, lumped-element investigations have shown that when an ad-hoc pressure distribution representative of vortical loadings is applied to the vocal fold surface the influence on the resultant vocal fold dynamics is negligible [32]. Similarly, investigations of vortex-VF interactions using a potential flow model concluded that that the pressure signature arising from the vortex cores had a minimal influence on the vocal fold dynamics [33]. Unfortunately, the ad-hoc estimation of the vortex pressure loading [32], and the non-physiological insertion of the vortices into the flow field [33], does not allow for a definitive interpretation of how intra-glottal vortices influence vocal fold dynamics during normal voiced speech production. Consequently, the importance of vortical structures as an energy transfer mechanism for driving normal voiced speech production remains unresolved.

The current study builds upon previous work [34], where the fluid-structure interaction of a discrete vortex ring advecting tangentially over a cantilevered plate was investigated as a function of vortex separation distance from the plate. This study seeks to elucidate the impact of fluid loading periodicity on the dynamics of a flexible, cantilevered plate, with an emphasis on the time scales that govern the interaction when the vortex production frequency is not synchronized with the fundamental frequency of the plate. As such, the objectives of this study are to: (1) determine how discrete versus periodic vortex loading impacts the fluid-structure interactions for the scenario of vortex rings advecting tangentially over a cantilevered plate, which will be investigated for various plate configurations, specified by a non-dimensional mass parameter; (2) utilize the findings to gain insight into the fields of energy harvesting and voiced speech production. This formulation is particularly advantageous for investigating the influence of vortex advection over the vocal fold surface on phonatory dynamics, as it allows the vortex loading to be decoupled from the aerodynamic loading of the bulk fluid flow; a capability that has not been achievable to date.

The manuscript is outlined as follows: the problem formulation is introduced in §2, the experimental methods are presented in §3, results are discussed in §4, and §5 is left for the conclusions.

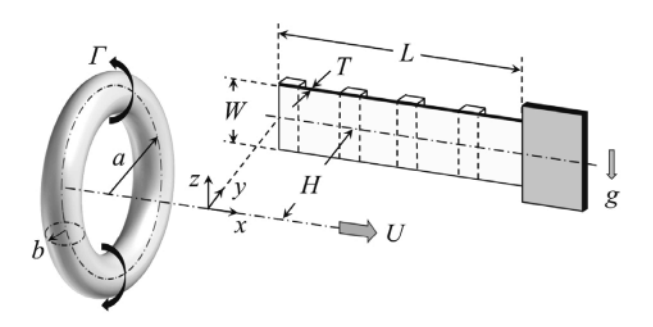


Fig. 1. Schematic of the vortex ring and cantilevered plate configuration.

2. Problem formulation

In the current study, the tangential advection of periodically-generated vortex rings over a cantilevered flexible plate is investigated. The relevant parameters of the plate and the coordinate system are shown in Fig. 1, where the plate length, width, and thickness are denoted by L, W, and T, respectively. The vortex ring advects over the plate surface with initial velocity U, radius a, core radius b, and circulation Γ . The coordinate system is chosen such that the x-axis (see Fig. 1) is located on the initial ring centerline, and is parallel to the plate centerline, with x=0 aligned with the plate tip. The ring moves in the positive x-direction, from the plate tip (the free end) to the plate base (the fixed end). The plate centerline vibrates in the y-direction in the x-y plane, and perpendicular to gravity (negative z-direction), such that body forces on the plate are negligible. The distance between the plate surface and the ring centerline is denoted by H.

2.1. Governing equations

If the plate length-to-thickness ratio is large, and the plate undergoes pure cylindrical bending with small vibration amplitude, the dynamics can be modeled using Kirchhoff-Love plate theory [35], which is governed by

$$m_{\rm s} \frac{\partial^2 \delta}{\partial t^2} + K \frac{\partial^4 \delta}{\partial x^4} + C \frac{\partial \delta}{\partial t} = [\![p]\!](x,t), \tag{1}$$

where $\delta(x,t)$ is the deflection of the plate from its rest position [m], m_s is the total mass per unit area of the plate [kg · m⁻²], K is the plate flexural rigidity per unit width [N · m], C is the plate structural damping coefficient per unit area [kg · s⁻¹ · m⁻²], and [[p]](x,t) is the pressure difference across the upper (facing toward the vortex ring; -y plane) and lower (facing away from the vortex ring; +y plane) surfaces of the plate [Pa]. To enable modification of the plate mass, additional material is attached to the side of the plate opposite the vortex rings. The dimensions and quantity of the added material are determined based on the desired mass per unit area (m_s) of the plate. Each section of added mass spans the entire plate width (W) and the spacing is selected such that the effect on the plate stiffness is negligible, which was confirmed through experiments.

Using L as the length-scale, U as the velocity scale, the vortex ring advection time $T_a = L/U$ as the time-scale, and $p_0 = \rho U^2$ as the pressure-scale, where ρ is the fluid density, Eq. (1) can be non-dimensionalized into

$$\Pi_{\mathbf{m}} \frac{\partial^2 \delta^*}{\partial t^{*2}} + \Pi_{\mathbf{s}} \frac{\partial^4 \delta^*}{\partial x^{*4}} + \Pi_{\mathbf{d}} \frac{\partial \delta^*}{\partial t^*} = \llbracket p^* \rrbracket (x^*, t^*), \tag{2}$$

where $\Pi_{\rm m}=m_{\rm s}/\rho L$ is a non-dimensional mass parameter, $\Pi_{\rm s}=K/\rho U^2L^3$ is a non-dimensional stiffness parameter, and $\Pi_{\rm d}=C/\rho U$ is a non-dimensional damping parameter. Superscript * indicates a non-dimensional variable, e.g., $\delta^*=\delta/L$. The pressure loading on the plate due to an advecting vortex ring is a function of the ring properties, plate dimensions, and their relative distance such that

$$[p^*] = f(H^*, a^*, b^*, \Gamma^*, Re, AR),$$
 (3)

where $H^* = H/L$ is the non-dimensional distance of the vortex ring from the plate, $a^* = a/L$ is the non-dimensional radius of the ring, $\Gamma^* = \Gamma/(UL)$ is the non-dimensional vortex ring circulation, $R = \Gamma/\nu$ is the vortex ring Reynolds number, where ν is the kinematic viscosity of the fluid, and AR = W/L is the plate aspect ratio. Because the pressure loading is a function of both H^* and A^* , it is advantageous to express the separation distance between the plate and the rings in terms of $H^*/A^* = H/A$.

There are three primary time-scales present in the problem: (i) the fundamental period of plate oscillation $T_0 = 1/f_0$, where f_0 is the fundamental frequency of plate oscillation; (ii) the vortex ring advection time-scale that specifies the time required for the vortex to advect one plate length, $T_a = L/U$; and (iii) the period of vortex ring production $T_p = 1/f_p$, where f_p is the frequency at which a train of periodic vortices is created. Based on these time-scales, two non-dimensional time parameters are defined. The first is the Strouhal number, given as

$$St = \frac{T_a}{T_0} = \frac{f_0 L}{U}.$$
 (4)

The St number defines the fraction of the plate fundamental period that a vortex ring takes to advect over the plate. St < 1 indicates that the duration for which the vortex ring applies a load to the plate is smaller than the plate's fundamental period of oscillation. For sufficiently small values (St << 1) the load is similar to an impulse; for St > 1, the load applied by the vortex ring occurs for a longer duration than the fundamental period of the plate.

The natural frequencies of a cantilevered plate undergoing pure cylindrical bending can be expressed as

$$f_{\rm n,i} = \frac{1}{2\pi} \left(\frac{\beta_{\rm i}}{L}\right)^2 \sqrt{\frac{K}{m_{\rm s}}}.\tag{5}$$

The fundamental frequency is defined as the first natural frequency ($f_0 = f_{n,1}$). In Eq. (5), β_i is the coefficient of the i-th mode of vibration, which is equal to 1.875 for the fundamental mode [35]. After some algebraic manipulation, Eq. (5) can be written as

$$St = \frac{\beta_i^2}{2\pi} \sqrt{\frac{\Pi_s}{\Pi_m}},\tag{6}$$

which shows that the St number can also be expressed as a function of the mass and stiffness parameters, and therefore plays an important role in defining the plate dynamics.

The second non-dimensional time parameter is the ratio of vortex ring production frequency to the plate fundamental frequency, defined as a frequency ratio

$$f^* = \frac{f_{\rm p}}{f_{\rm o}} = \frac{T_{\rm o}}{T_{\rm p}}.\tag{7}$$

A value of $f^* < 1$ signifies that the duration between two consecutive vortices is longer than the fundamental period, and the plate oscillations will begin to decay before the subsequent vortex arrives. A value of $f^* \simeq 1$ signifies that the plate is set into motion by the incoming train of vortices at resonance conditions. For $f^* > 1$, more complex oscillations are expected to arise as higher modes of plate oscillation are activated.

2.2. Range of parameters

Structural and aerodynamic damping in the current study that is performed in air were small, as evidenced by a highly underdamped plate response during simple impulse response ("flick") tests. As such, Π_d in Eq. (2) is assumed negligible for all subsequent work. Although damping plays an important role in vocal fold oscillations, neglecting Π_d will simply provide an upper limit for the magnitude of the resultant plate oscillations. For a particular fluid loading $[p^*]$, the plate dynamics are determined by the relative influence of Π_m and Π_s , and, as such, plate properties can be altered by changing one of the parameters. The range of values of Π_s and Π_m found in both energy harvesting and voiced speech investigations are displayed on a logarithmic scale in Fig. 2. Black squares denote experiments performed in water, red circles denote experiments in air, and the blue triangles outline the limits for voiced speech production. The numbers in the brackets reference the corresponding

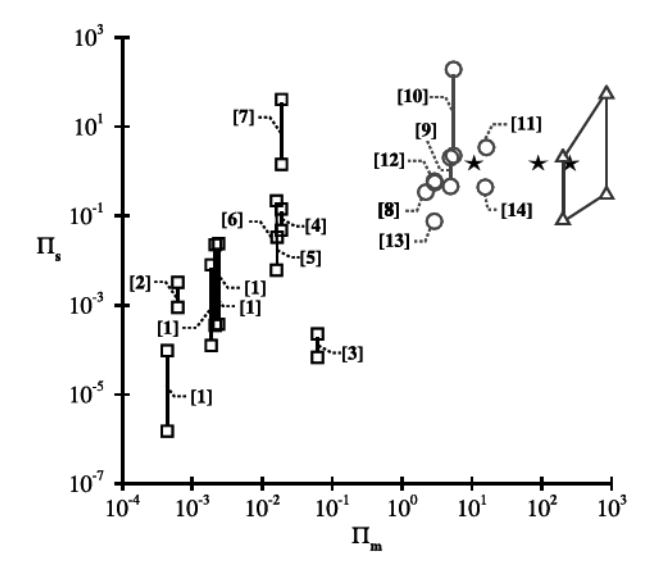


Fig. 2. The range of mass and stiffness parameters in energy-harvesting investigations in water (□) and air (O). The numbers in the brackets represent the corresponding articles listed in Table 1. Investigations that considered a range of parameters are connected by a line. △ connected by lines represents the bounds of structural vocal fold parameters found in voiced speech. ★ represent the cases investigated in the current study.

Energy narvesting studies and the respective fluid medium corresponding to the numbers in brackets snown on Fig. 2.						
Article No.	Authors	Medium	Article No.	Authors	Medium	
[1]	Allen and Smits [19]	Water	[8]	Akaydin et al. [9]	Аіг	
[2]	Taylor et al. [13]	Water	[9]	Akaydin et al. [18]	Аіг	
[3]	Giacomello and Porfiri [14]	Water	[10]	Akaydin et al. [15]	Аіг	
[4]	Peterson and Porfiri [20]	Water	[11]	Hobeck and Inman [36]	Аіг	
[5]	Zivkov et al. [21]	Water	[12]	Goushcha et al. [23]	Аіг	
[6]	Wang et al. [37]	Water	[13]	Orrego et al. [38]	Аіг	
[7]	Cha et al. [10]	Water	[14]	Gao et al. [39]	Аіг	

Table 1Energy harvesting studies and the respective fluid medium corresponding to the numbers in brackets shown on Fig. 2.

studies listed in Table 1, Individual studies that investigate multiple plate/fluid properties are connected by a line with the end points spanning the range of investigated values. For example, Allen and Smits [19] investigated four different membranes with different dimensions over a range of free-stream velocities. It should also be noted that increased fluid density yields a lower mass parameter, as visible by comparing studies in air (denoted by red circles) and water (denoted by black squares) in Fig. 2.

For voiced speech production, an order of magnitude estimation of mass and stiffness parameters can be computed from known values of the vocal fold structure. The flexible membrane of the vocal folds that undergoes oscillations during voiced speech is often referred to as the cover layer [40]. The portion of the cover layer that is subjected to fluid loading is reported to have a length of approximately 1.0–3.0 mm [41], a width of 12–17 mm [42], and a thickness of 0.50–1.0 mm [43], with a tissue density of $\rho_{\rm t}=1,030~{\rm kg\cdot m^{-3}}$ [44]. The transverse modulus of elasticity of the vocal folds, which is aligned with the primary direction of vocal fold oscillations, has been reported as 1.00–20.0 kPa [44]. Based on these values, the bounds for the mass and stiffness parameters are calculated and denoted by blue triangles in Fig. 2.

In the current study, the influence of variable frequency pressure loading is investigated for three cantilevered plates; all plates have the same stiffness parameter ($\Pi_s \simeq 1.48$), but with varying values of mass parameter ($\Pi_m = 11.4, 95.1$, and 251). These values represent plates with parameters that span the range of applications in air from voiced speech to energy harvesting. The location of these plate parameters in the $\Pi_s - \Pi_m$ map are denoted by black stars in Fig. 2. Because the non-dimensional stiffness parameter of the three plates is the same, in future discussions they will be differentiated simply by referring to their non-dimensional mass parameter, Π_m .

3. Experimental methods

The experimental facility and procedures are briefly described herein. For a more detailed description, see Pirnia et al. [34].

3.1. Experimental facility

An 8in. Morel subwoofer was housed in a cylindrical plenum, with an attached d=24 mm ID circular tube, see Fig. 3(a). Air was pushed out of the plenum by the movement of the speaker cone, producing a vortex ring. The ring circulation, and thus its advection velocity, was adjusted by a variable sawtooth signal (short rising and long settling duration), that was created in National Instruments (NI) LabVIEW® software and amplified with a Kepco BOP-36 amplifier.

With the aim of maximizing the energy of each vortex ring, the speaker cone displacement was controlled to achieve a formation number of approximately 4 for all rings [45]. To achieve this formation number, the speaker cone movement amplitude was set at 2.0 mm for the effective cone diameter of 160 mm. The vortex production system can be used to generate either a discrete vortex or a periodic chain of vortices at the vortex production frequency f_D .

Three plates were fabricated from polycarbonate sheets with dimensions listed in Table 2 and placed downstream of the tube with a cantilevered type support such that their tip (free end) was facing the incoming vortex rings. The support is held in place by a 0.50 inch aluminum rod and a base plate that is bolted to an optical table. In this manner, the stiffness of the support structure was approximately 4 orders of magnitude larger than the vibrating plates. All plates had identical widths

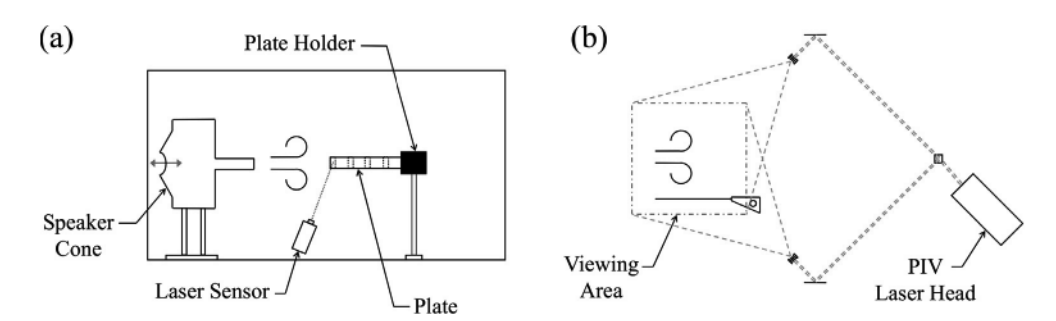


Fig. 3. Schematic of the experimental facility: (a) vortex production plenum and plate configuration; and (b) laser sheet alignment and viewing area for PIV measurements.

Table 2Properties of the plates used in the experiments.

Description	Variable	$\Pi_{\rm m}=11.4{ m Value}$	$\Pi_{\rm m}=95.1{ m Value}$	$\Pi_{\rm m}=251{ m Value}$	[Units]
Plate length	L	100 ± 0.1	80.0 ± 0.1	85.0 ± 0.1	[mm]
Plate width	W	25.0 ± 0.1	25.0 ± 0.1	25.0 ± 0.1	[mm]
Plate thickness	T	0.250 ± 0.010	0.250 ± 0.010	0.250 ± 0.010	[mm]
Mass per unit area	m_s	1.40 ± 0.01	9.32 ± 0.06	26.2 ± 0.30	[kg/m ²]
Flexural rigidity per unit width	K	3.42 ± 0.10	3.33 ± 0.30	4.53 ± 0.30	10 ⁻³ [N · m]
Fundamental frequency	f_{o}	2.71 ± 0.01	1.61 ± 0.06	1.02 ± 0.04	[Hz]

and thicknesses with lengths L=100 mm, 80.0 mm, and 85.0 mm for plates with $\Pi_{\rm m}=11.4$, 95.1, and 251, respectively. Mechanical properties of the plates were derived from 100 impulse response (flick) tests per plate and are reported in Table 2 along with their standard deviations. A scale with 0.1 g resolution was used for determining the mass per unit area, $m_{\rm s}$, of the plates. Note that both $\Pi_{\rm s}$ and $\Pi_{\rm m}$ are functions of the plate length, while only $\Pi_{\rm s}$ is a function of vortex advection velocity. Due to limitations in the achievable advection velocity of the facility, it was therefore necessary to modify the plate length as well as the vortex ring advection velocity to achieve the desired variations in $\Pi_{\rm m}$ while maintaining a constant $\Pi_{\rm s}$.

The offset distance of the plate from the vortex centerline was fixed at $H_0^*/a^* = 1.37$; this spacing was previously found to result in the maximum vibration amplitude [34]. At this offset distance, a portion of the vortex ring core is tangent to the plate surface at $x^* = 0$ when the plate is stationary. A Wenglor PNBC005 laser displacement sensor was used to record the instantaneous deflection at the plate tip, with a sampling frequency of 10 kHz and a resolution of 1.5 μ m. The signal was acquired with a NI 6320 DAQ card and processed with NI LabVIEW® software. All of the deflection measurements were performed after the steady-state oscillation of the plates were reached, and were averaged over 100 fundamental periods to ensure repeatability of the results.

A closed $610 \text{ mm} \times 610 \text{ mm} \times 1220 \text{ mm}$ acrylic box surrounded the entire system (speaker, plenum, and plate) to isolate the flow field from ambient room eddies and contain the flow seeding particles; the box was sufficiently large to minimize any effect of the walls on the flow field.

3.2. Flow measurement

A LaVision Flow Master particle image velocimetry (PIV) system was used to measure the velocity fields. A custom fabricated olive oil atomizer generated the seed particles. In similar systems, the particle sizes were reported to be $\mathcal{O}(1-10)\,\mu\mathrm{m}$ [46]. A 532 nm Nd:YAG (Litron Nano L) laser beam was divided with a beam splitter and passed through a mirror-cylindrical lens combination, as shown in Fig. 3(b), to evenly illuminate both sides of the cantilevered plate. Precise alignment of the laser sheet with the plate and vortex ring centerlines minimized out-of-plane velocity gradients. Phase-locked image pairs of the vortex rings were acquired with a 2560 \times 2160 pixel Image sCMOS camera at full resolution. It was found that averaging 50 image pairs was sufficient to ensure convergence of the mean flow field to within 2.5% over the entire domain.

To ensure that the maximum particle displacement between image pairs was approximately one-quarter of the final interrogation region size of 32×32 pixels, the laser timing was optimized for each plate/vortex ring combination as $dt=240~\mu s$, $180~\mu s$, and $170~\mu s$ for values of $\Pi_m=11.4$, 95.1, and 251, respectively. With 75% window overlap, the spatial resolution was 0.5~mm, which corresponds to a spatial resolution non-dimensionalized by plate length of $\Delta x^*=5\times 10^{-3}$, 6×10^{-3} , and 6×10^{-3} for the plates with $\Pi_m=11.4$, 95.1, and 251, respectively. PIV data were acquired at 5 instances in time as the vortex rings advected over the plate, corresponding to non-dimensional times ranging from $t^*=0$ to 1 with a non-dimensional time increment of 0.25, where $t^*=0$ corresponds to the time when the vortex ring was aligned with the plate tip. Laser reflections at the plate surface were eliminated by background subtraction from each image pair and geometric masking of the plate and its holder before processing. The image capture, timing, and data processing were performed with the DaVis 8 software package on a PC with $2\times$ quad-core XEON processor with 12~GB of RAM.

The speaker (vortex generator) input signal, PIV triggering, and data acquisition from the laser displacement sensor were handled and synchronized with NI LabVIEW® software. A NI USB-6001 DAQ card created the speaker and trigger signal with the required vortex ring production frequency, f_p . The frequency ratio was varied in the range of $0.010 < f^* < 1.6$. The properties of the undisturbed vortex rings for the three cases of interest were first measured without the cantilevered plate to quantify the vortex ring properties. The properties were averaged from 250 trials over all 5 instances in time and are presented in Table 3, along with their standard deviations, revealing largely constant ring properties over the domain of interest. In particular, the standard deviation of the ring and core radii of the free vortices was less than 2%, indicating the ring advection velocity was only a function of the ring circulation. The advection velocity was measured to be $U=1.35 \, \text{m/s}$, $1.84 \, \text{m/s}$, and $2.00 \, \text{m/s}$ for the cases of $\Pi_m=11.4$, 95.1, and 251, respectively. The Reynolds number of the vortex rings utilized in the current study, shown in Table 3, indicate laminar vortex rings [47] for all cases.

In order to achieve the required vortex ring circulation in each case, the duration of the rising portion of the incoming signal to the speaker was set to be 54 ms, 35 ms, and 32 ms, for the plates with $\Pi_{\rm m}=11.4,95.1$, and 251, respectively. The vortex ring circulation was calculated by area integration of vorticity inside the outermost closed contour of vorticity near each vortex core. The value of vorticity at the closed contour varied for the three plates from $\omega_z^*=22.2,13.0$, and 13.5 in the beginning, where the

Description	Variable	$\Pi_{\rm m}~=~11.4~{\rm Value}$	$\Pi_{\rm m}=95.1{ m Value}$	$\Pi_{\rm m}=251{ m Value}$	[Units]
Circulation	Γ	9.00 ± 1.00	13.0 ± 2.00	15.0 ± 2.00	10 ⁻² [m ² /s]
Advection velocity	U	1.35 ± 0.01	1.84 ± 0.02	2.00 ± 0.02	[m/s]
Ring radius	а	18.2 ± 0.3	18.5 ± 0.3	18.6 ± 0.3	[mm]
Core radius	b	6.8 ± 0.1	6.3 ± 0.1	6.2 ± 0.1	[mm]
Mass parameter	Π_{m}	11.4 ± 0.12	95.1 ± 1.2	251 ± 6.3	
Stiffness parameter	П,	1.45 ± 0.03	1.46 ± 0.10	1.51 ± 0.09	
Damping parameter	Π_d	0.10 ± 0.01	0.31 ± 0.05	0.37 ± 0.11	
Reynolds number	Re	5.5 ± 0.1	7.9 ± 0.1	9.1 ± 0.1	$\times 10^3$
Strouhal number	St	0.20 ± 0.010	0.070 ± 0.010	0.040 ± 0.010	

Table 3Properties of the vortex rings produced in the experiments and the corresponding non-dimensional parameters.

vortex ring was formed, to $\omega_z^* = 3.70$, 2.17, and 2.20 in the end, where the vortex ring dissipated, for values of $\Pi_m = 11.4$, 95.1, and 251, respectively. Prior investigations, not shown here for brevity, determined that the vortex rings achieved their maximum circulation at $x^* = t^* = 0.20$, 0.13, and 0.15 for the corresponding plates with $\Pi_m = 11.4$, 95.1, and 251, respectively. The change in vortex ring circulation over the length of the plate was approximately 15%.

3.3. Pressure estimation

The pressure field was calculated from the measured PIV velocity fields to determine the load applied to the plates. Following Pirnia et al. [34], the pressure was estimated by solving the pressure Poisson equation using a technique that is similar to that proposed by Shams et al. [48]. Specifically, a conservative form of the pressure Poisson equation that includes the velocity derivatives in all three directions

$$\frac{\partial^2 p}{\partial x^2} + \frac{\partial^2 p}{\partial y^2} = -\rho [g_1(x, y, t) + g_2(x, y, t) + g_3(x, y, t)],\tag{8}$$

was employed, where the source terms are

$$g_{1}(x,y,t) = \left(\frac{\partial u}{\partial x}\right)^{2} + 2\frac{\partial u}{\partial y}\frac{\partial v}{\partial x} + \left(\frac{\partial v}{\partial y}\right)^{2},$$

$$g_{2}(x,y,t) = \frac{\partial}{\partial t}\left(\frac{\partial u}{\partial x} + \frac{\partial v}{\partial y}\right) + u\frac{\partial}{\partial x}\left(\frac{\partial u}{\partial x} + \frac{\partial v}{\partial y}\right) + v\frac{\partial}{\partial y}\left(\frac{\partial u}{\partial x} + \frac{\partial v}{\partial y}\right),$$

$$g_{3}(x,y,t) = w\frac{\partial}{\partial z}\left(\frac{\partial u}{\partial x} + \frac{\partial v}{\partial y}\right) + \frac{\partial w}{\partial x}\frac{\partial u}{\partial z} + \frac{\partial w}{\partial y}\frac{\partial v}{\partial z},$$

$$(9)$$

and u, v, and w are flow velocity components in the x-, y-, and z-directions, respectively. Viscous stress terms were found to have negligible contribution to the results and were thus ignored in the estimation process.

The g_2 and g_3 terms in Eq. (9) include the out-of-plane velocity component, w, and its derivatives. The terms in g_2 were calculated from known two-dimensional PIV data, but the required information for calculating the terms in g_3 were not available. As such, the contribution of g_3 to the pressure field was neglected and considered a source of error.

A central difference scheme was used for solving Eq. (8) at the interior nodes. PIV velocity fields were acquired 2 ms before and after each of the 5 instances in time that are of interest to provide the required information for calculating the time derivatives. An Immersed Boundary method with a three-point interpolation was employed along the moving boundary (the plate) [49]. The known velocity and acceleration of the plate measured by the laser displacement sensor were used in the calculation of normal pressure gradients at the boundary.

4. Results and discussion

The dynamics of the three plates subject to loadings produced by discrete and periodic trains of vortices are discussed in §4.1, the differences between the dynamics and fluid loading of the three plates at resonance are explained in §4.2, applications to the energy harvesting are investigated in §4.3, and the flow field and plate dynamics with application to voiced speech production are discussed in §4.4.

4.1. Plate dynamics arising from discrete and periodically-generated vortices

The steady-state plate tip deflection ($\delta_{\rm tip}^*$) time series at frequency ratios of $f^*=0.010$, 0.50, and 1.0 with $\Pi_{\rm m}=11.4$ are shown in Fig. 4. The time series are displayed spanning one, two, and four periods of vortex production ($T_{\rm p}^*=[f^*{\rm St}]^{-1}$) for the three frequency ratios, respectively.

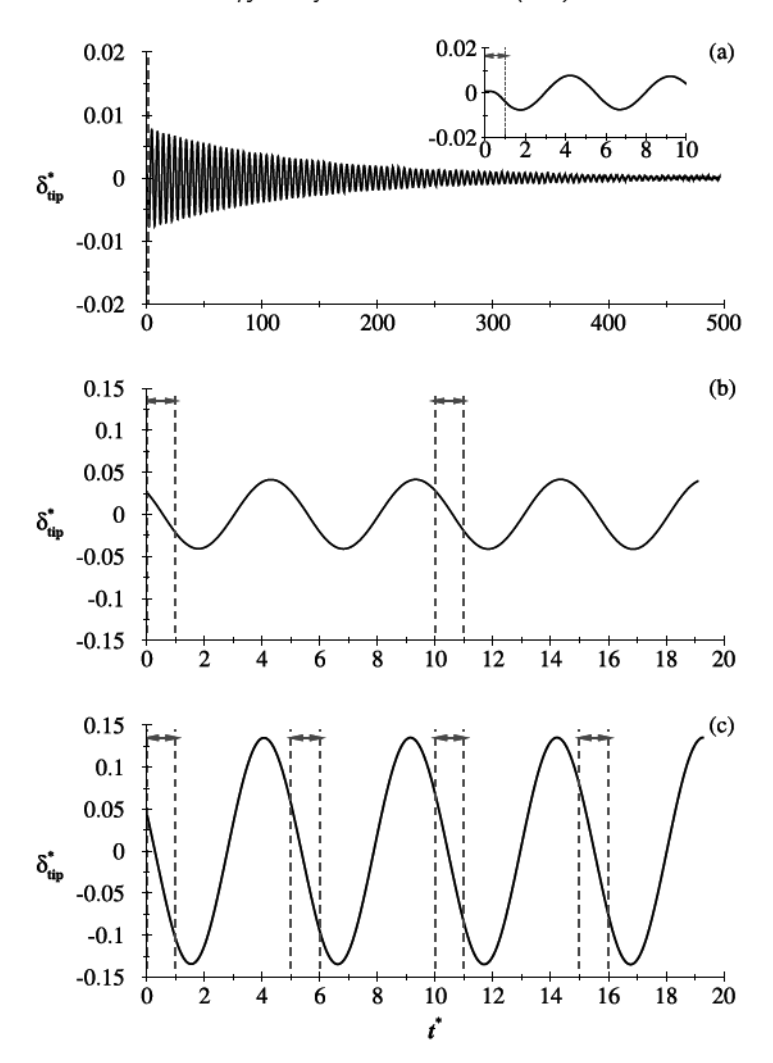


Fig. 4. Non-dimensional plate tip deflection time series at $H_0^*/a^* = 1.37$ for the plate with $\Pi_m = 11.4$ at (a) $f^* = 0.010$, (b) $f^* = 0.50$, and (c) $f^* = 1.0$.

The areas between the dashed vertical red lines (marked with arrowheads) in Fig. 4 denote the time during which the vortex rings advect over the plate ($0 \le t^* \le 1$, etc.). The time history of Fig. 4(a) is shown for a discrete vortex loading ($f^* = 0.010$). The inset shows a zoomed-in view of the vortex loading duration relative to the plate response. The discrete vortex ring sets the plate into oscillation when it is effectively at rest ($\delta^* < 0.1\%$), after which, the plate exhibits an underdamped response. The propagation time of the vortex passing over the plate is very short relative to the asymptotic decay of the plate. The steady-state vibrations at $f^* = 0.50$ and $f^* = 1.0$ in Fig. 4(b) and (c) show that the oscillations are phase-aligned such that when a vortex approaches the plate tip, the plate is deflected away from the vortex (in the +y-direction) (refer to Fig. 1), but moving towards the vortex ring (in the -y direction). Interestingly, the duration of the vortex loading on the plate spans a time centered roughly about the rest position of the plate. For $f^* = 0.50$ and $f^* = 1.0$, the fluid loading on the plate occurs over a small fraction of the plate's fundamental period of oscillation due to the small Strouhal number. For values of $f^* < 1.0$, the maximum plate amplitude occurs during the cycle following the advection of the vortex ring, after which the deflection time history decays gradually until the subsequent vortex ring arrives. Because the vortex rings arrive at every other fundamental period of oscillation for $f^* = 0.50$ in Fig. 4(b), the deflection amplitude is less than half of the amplitude reached when the plate is driven at resonance ($f^* = 1.0$ in Fig. 4(c)).

A plot of the maximum non-dimensional plate tip deflection, $\delta^*_{\rm tip,max}$, as a function of f^* is shown in Fig. 5. The blue triangles represent the plate with $\Pi_{\rm m}=11.4$, the red squares represent the plate with $\Pi_{\rm m}=95.1$, and the black circles represent the plate with $\Pi_{\rm m}=251$. The plates are subjected to a train of vortices at different non-dimensional frequencies, ranging from $f^*\simeq 0.010$ to 1.6. The upper limit of f^* was constrained by the ability to produce unique vortices that did not interact with each other (e.g., experience "leap-frogging", etc. [50]). As such, interactions arising from higher non-dimensional frequencies were not explored.

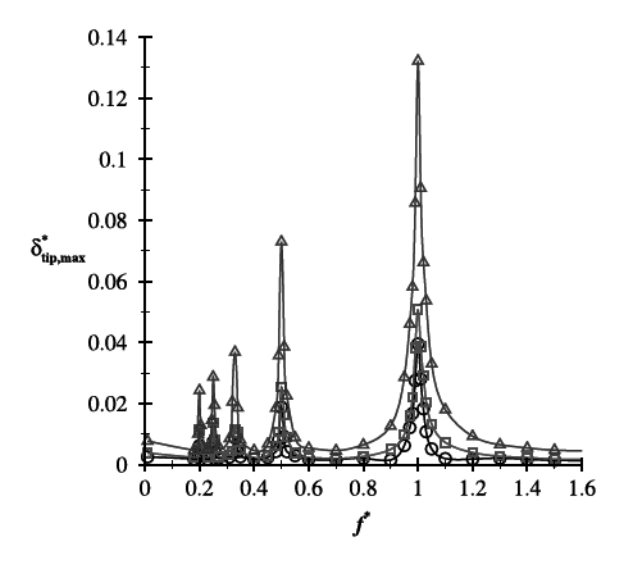


Fig. 5. Non-dimensional plate tip deflection as a function of the non-dimensional frequency ratio f^* at $H_0^*/a^*=1.37$, Δ represent $\Pi_{\rm m}=11.4$, \square represent $\Pi_{\rm m}=95.1$, and \bigcirc represent $\Pi_{\rm m}=251$.

As shown in Fig. 5, peaks in the maximum plate deflection occur when the vortex production frequency is a sub-harmonic of the plate fundamental frequency (i.e., $f^* = 1/1$, 1/2, 1/3, 1/4, etc.). Due to the small Strouhal number in all three cases (St < 0.20, refer to Table 3), the fluid loading acts as an impulse and amplifies the plate oscillations if it is applied at an integer multiple of the fundamental period of the plate. Although an infinite number of sub-harmonics of the fundamental frequency occur between $0 < f^* < 1$, only four were investigated, and are shown in Fig. 5. The displacement due to a discrete vortex

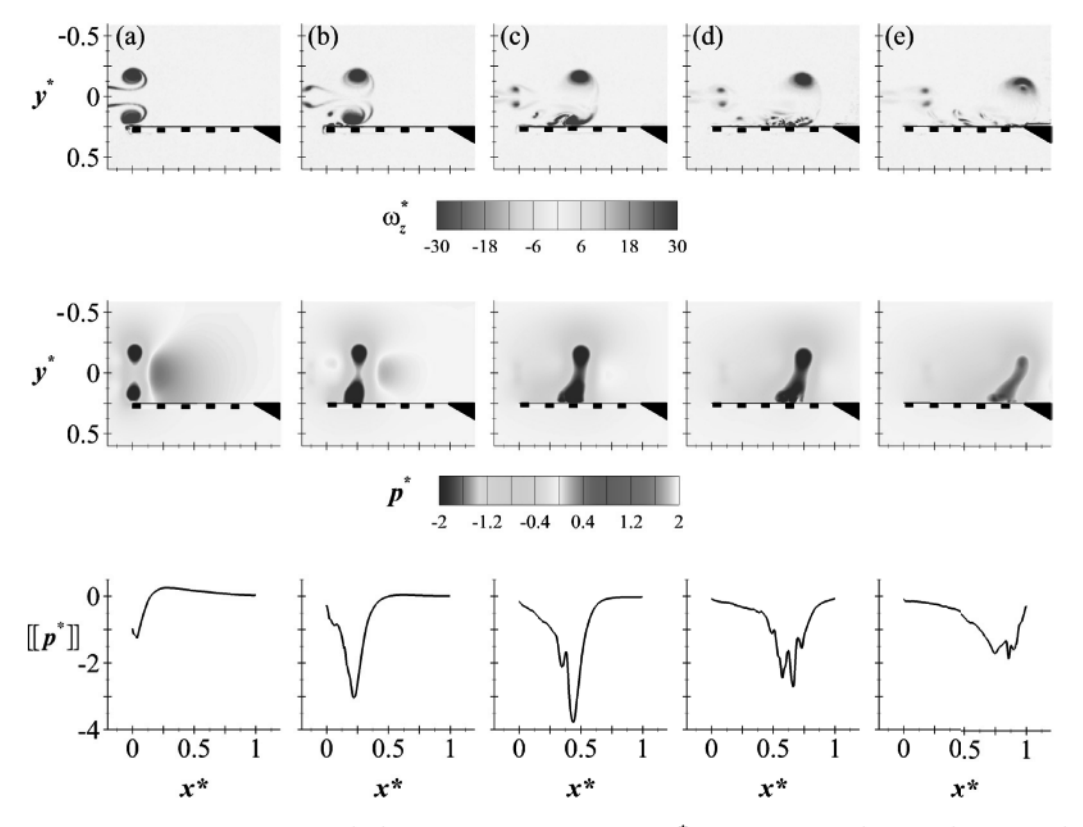


Fig. 6. Derived values from PIV data at a distance ratio of $H_0^*/a^* = 1.37$ for a plate with $\Pi_m = 11.4$ at $f^* = 0.010$ at times (a) $t^* = 0$, (b) $t^* = 0.25$, (c) $t^* = 0.50$, (d) $t^* = 0.75$, (e) $t^* = 1.0$. Top row – vorticity contours, middle row – pressure contours, bottom row – resultant pressure difference across the plate.

ring can be considered for $f^* = 2/201$, where the temporal spacing between successive rings is not an integer multiple of the fundamental plate period, and sufficient time passes between consecutive vortices (e.g., ~ 37 s for the plate with $\Pi_{\rm m} = 11.4$) for the plate oscillations to be completely damped out.

As expected, the oscillation amplitudes are a function of the non-dimensional plate mass, with lower values yielding higher displacements. For a discrete vortex advecting over the plate with $\Pi_{\rm m}=11.4$, the maximum plate deflection at the tip is $\delta^*_{\rm tip,max}=8.0\times 10^{-3}$, compared to $\delta^*_{\rm tip,max}=4.0\times 10^{-3}$, and 3.0×10^{-3} for the plates with $\Pi_{\rm m}=95.1$ and $\Pi_{\rm m}=251$, respectively. When the plate fundamental frequency and vortex production frequency match ($f^*=1.0$), the maximum tip displacement increases by approximately an order of magnitude to $\delta^*_{\rm tip,max}=130\times 10^{-3}$ for the plate with $\Pi_{\rm m}=11.4$, compared to $\delta^*_{\rm tip,max}=51.0\times 10^{-3}$, and 39.0×10^{-3} for the plates with $\Pi_{\rm m}=95.1$ and $\Pi_{\rm m}=251$, respectively. To provide a clear picture of the effect of vortex interactions with the plate, vorticity and pressure contours over the plate with $\Pi_{\rm m}=11.4$ are derived from recorded PIV data at 5 instances in time. Results are shown in Fig. 6 for discrete vortices ($f^*=0.010$) and in Fig. 7 for a train of vortices at resonance ($f^*=1.0$).

The interactions of discrete vortices with a flexible plate has previously been discussed in detail [34]. At $f^* = 0.010$, the plate is initially deflected slightly away from the vortex (+y-direction) due to downwash from the incoming vortex, as visible in Fig. 4(a), and evidenced by the positive pressure loading peak in the bottom panel of Fig. 6(a). As the vortex ring advects over the surface the negative gauge pressure in the vortex core pulls the plate in the -y-direction. As the vortex progresses over the plate, vorticity interactions occur between the vortex ring and: (i) induced vorticity on the plate surface; and (ii) a tip vortex arising from the initial plate displacement. The resultant opposite-sign vorticity interactions weaken the vortex ring and deflect it towards the plate surface (Fig. 6(a)-(c)). Ultimately, the vortex ring is annihilated (Fig. 6(d)-(e)).

For vortex loading corresponding to $f^* = 1.0$, the mechanics of the interaction are the same, but the plate is initially deflected away from the ring, as observed in Fig. 7(a), due to the transient vibrations that persist from the previous oscillation. Consequently, the pressure load is initially smaller (see Fig. 7, bottom row) when compared with Fig. 6 due to the larger distance between the ring and the surface, and the total load experienced by the plate is smaller as well. However, this change in relative vortex-to-plate spacing due to the steady-state plate oscillation has a significant impact on the magnitude of the loadings that are exerted on the plate.

The instantaneous separation distance between the vortex ring and the plate with $\Pi_{\rm m}=11.4$ and $H_0^*/a^*=1.37$ at the three investigated frequency ratios is shown in Fig. 8(a). The ratio h_1/a , expresses the distance between the center of the por-

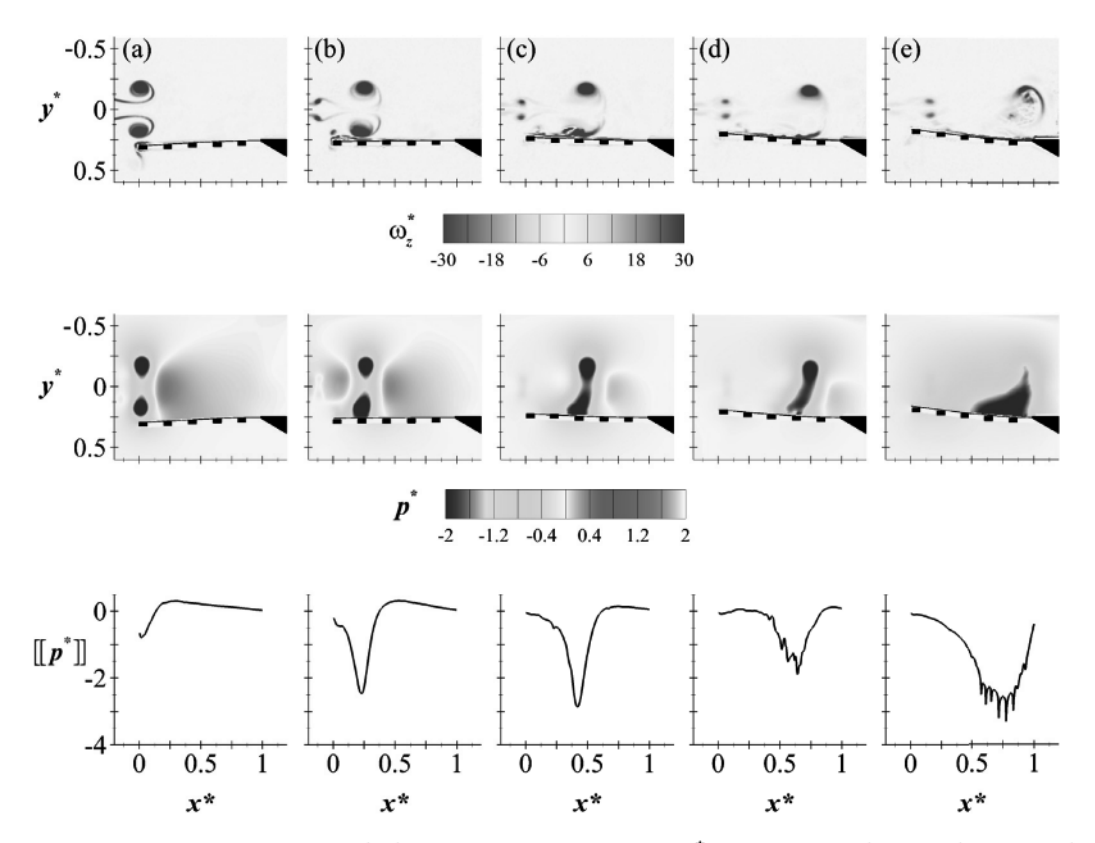


Fig. 7. Derived values from PIV data at a distance ratio of $H_0^*/a^* = 1.37$ for a plate with $\Pi_m = 11.4$ at $f^* = 1.0$, at times (a) $t^* = 0$, (b) $t^* = 0.25$, (c) $t^* = 0.50$, (d) $t^* = 0.75$, (e) $t^* = 1.0$. Top row – vorticity contours, middle row – pressure contours, bottom row – resultant pressure difference across the plate.

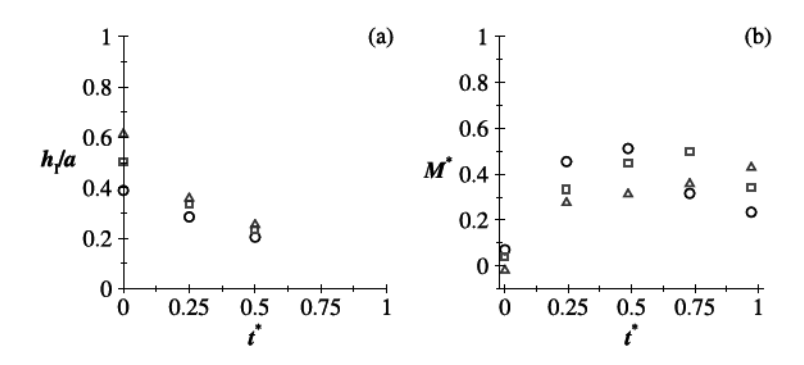


Fig. 8. a) Non-dimensional lower core separation distance from the plate surface, and b) non-dimensional applied moment at the base of the plate with $\Pi_m = 11.4$ over the duration $0 \le t^* \le 1$ at $H_n^*/a^* = 1.37$, \bigcirc represent $f^* = 0.010$, \square represent $f^* = 0.50$, and \triangle represent $f^* = 1.0$.

tion of the vortex ring core nearest the plate, referred to hereafter as the "lower vortex ring core", and the plate surface, non-dimensionalized by the vortex ring radius. For all frequency ratios, diffusion of the plate vorticity into the flow field quickly gives rise to vortex breakdown (see Fig. 6(d)-(e) and Fig. 7(d)-(e)). As such, the position of the lower vortex ring core is difficult to discern after $t^* = 0.5$, and consequently, the separation distance at these latter points is not shown in Fig. 8(a). It can be observed from Fig. 8(a) that the initial separation distance is larger at $f^* = 1.0$ than $f^* = 0.50$ and $f^* = 0.010$, but all approach zero as the vortex rings advect over the plate surface.

The non-dimensional moment produced by the vortex ring at the base of the plate is also shown in Fig. 8(b) for the three frequency ratios. The moment is expressed as the non-dimensional applied moment per unit width at the base of the plate, M_z^* , calculated as,

$$M_{z}^{*} = -\int_{0}^{1} [[p^{*}]](1-x^{*}) dx^{*}.$$
 (10)

A positive pressure difference across the plate produces a negative (CW) moment at the base of the plate, and vice versa, as defined by the coordinate system in Fig. 1. The non-dimensional applied moment is computed from the spatially-averaged pressure loading at each instance in time.

As the vortex ring advects over the first half of the plate, the resultant magnitude of the applied moment is dominated by the relative spacing between the ring and the plate, as can be observed by comparing Fig. 8(a) with Fig. 8(b), where increased vortex core to plate spacing produces a lower moment, and vice versa. This variation in relative vortex core to plate spacing arises due to the steady-state plate oscillations that persist from one loading cycle to the next. For small-amplitude oscillations (see Fig. 4(a) and Fig. 8(a) at $f^* = 0.010$) plate deflections are small and the subsequent vortex-to-plate spacing is small as well. As a result, following the initial downwash of the incoming vortex ring, the resultant plate moment is dominated by the low pressure in the core of the vortex. (see Fig. 8(b)). For higher steady-state amplitude oscillations (see Fig. 4(b) and (c) and Fig. 8(b) at $f^* = 0.50$ and $f^* = 1.0$) the increased initial vortex-to-plate spacing causes the plate tip loading to initially be lower.

As the vortex ring propagates over the latter half of the plate, the higher amplitude plate oscillations delay the time at which the maximum moment occurs. As previously reported [34], the spacing between the lower vortex ring core and the plate has a significant impact on the vortex dynamics, as the decreased spacing facilitates more robust interactions between the induced plate vorticity and the ring vorticity. Following the location of the peak non-dimensional moment on the plate, a significant decrease in the pressure loading occurs [34]. This behavior can be observed in Fig. 8(b) for $f^* = 0.010$, which corresponds to the lowest relative vortex-to-plate spacing, where a sudden decrease in the moment is experienced at $t^* = 0.75$. For the case of $f^* = 0.5$, the maximum moment and subsequent loss of loading occurs later in time ($t^* = 0.75$ and $t^* = 1.0$, respectively), likely due to the increased vortex-to-plate spacing which decreases the strength of the interactions between the vortex core and the wall vorticity. The highest steady-state oscillation amplitude, and subsequently the highest relative vortex-to-plate spacing, similarly exhibits an even more pronounced delay in the location of maximum loading.

For all three frequency ratios, the moment at the base of the plate is primarily positive, as shown in Fig. 8(b). When compared with the plate trajectories in Fig. 4 over the duration of $0 \le t^* \le 1$ (when the vortex ring is over the plate), it can be determined that for the steady-state oscillations the pressure loading occurs in phase with the plate motion. Furthermore, the time-average of the moment applied to the plate for the three different loading conditions shown in Fig. 8(b) is, interestingly, nearly the same; that is, $M_{\text{ave}}^* \simeq 0.31$ for all three frequency ratios, despite the temporal shift in the peak moment.

4.2. Influence of Strouhal number on plate dynamics

The maximum non-dimensional tip deflection of the three plates as a function of frequency ratio was shown in Fig. 5, exhibiting a peak at resonance. The steady-state deflection time series at resonance ($f^* = 1.0$) for non-dimensional plate mass

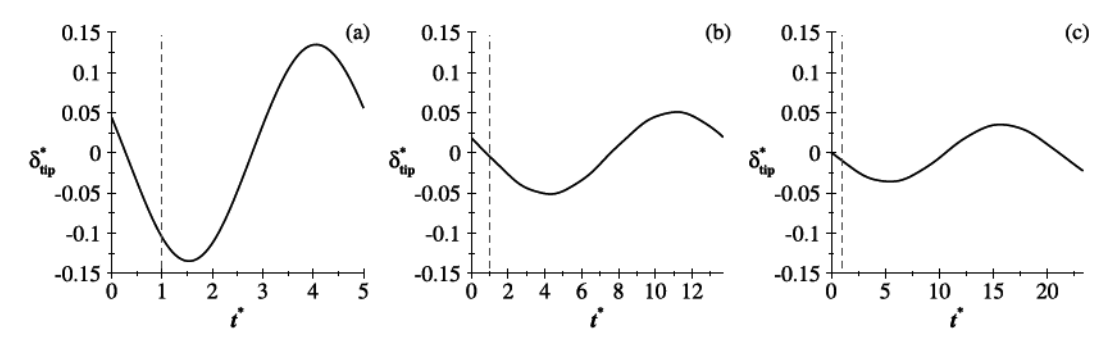


Fig. 9. Non-dimensional plate tip deflection time series at $H_0^*/a^* = 1.37$ and $f^* = 1.0$ for (a) $\Pi_m = 11.4$, (b) $\Pi_m = 95.1$, and (c) $\Pi_m = 251. \equiv 0$ denotes the time that the vortex ring is over the plate (0 $\leq t^* \leq 1$).

parameters of $\Pi_{\rm m}=11.4$, 95.1, and 251 are displayed in Fig. 9 over one period of oscillation, or vortex production period $(T_{\rm o}^*={\rm St}^{-1})$.

Just like the deflection time series in Fig. 4, all deflection diagrams in Fig. 9 are synchronized at $t^*=0$, where the vortex ring is at the tip of the plate and the plate is initially deflected away from the vortex ring, but rebounding towards it. The amplitude of the plate deflection depends on the non-dimensional mass parameter, with higher values corresponding to lower amplitudes. The area between $t^*=0$ and the red dashed vertical lines corresponds to the time it takes for the vortex ring to propagate over the plate. Note that in all instances this time is $t^*=1$, but the relative portion of the plate fundamental period over which the vortex loading applies decreases with increasing values of $\Pi_{\rm m}$. This ratio (the time the loading is applied to the plate divided by the period of plate oscillation) can be easily expressed as a Strouhal number according to Eq. (4), with corresponding values, reported in Table 3, of St = 0.20 for $\Pi_{\rm m}=11.4$, St = 0.070 for $\Pi_{\rm m}=95.1$, and St = 0.040 for $\Pi_{\rm m}=251$. In this manner, it is perhaps more meaningful to consider changes in energy loading as a function of Strouhal number. A higher value of Strouhal number indicates that the load is applied over a larger portion of each period of plate oscillation, thereby enabling the transfer of more energy to the plate on a per cycle basis.

The instantaneous distance between the lower vortex ring core and the plate surface is shown in Fig. 10(a), and the moment at the base of the plate at resonance ($f^* = 1.0$) is shown in Fig. 10(b) for the three non-dimensional mass parameters/Strouhal numbers. Just as was observed previously, where the peak in the moment is delayed for cases that produce higher amplitude oscillations (see Fig. 8(b)), increasing the Strouhal number, which increases the plate oscillation amplitude, delays the occurrence of the peak moment. The smallest plate displacement occurs for the case of St = 0.040 ($\Pi_{\rm m} = 251$), which also exhibits the earliest peak in the non-dimensional moment (see Fig. 8(b)) followed by a rapid decrease. The highest plate displacement, and latest peak in the non-dimensional moment, occurs for St = 0.20 ($\Pi_{\rm m} = 11.4$).

4.3. Plate energy

The total plate energy can be computed as the sum of the instantaneous strain, E_s , and kinetic, E_k , energies of the plate [21], where

$$E_{\rm s} = \frac{KW}{2L} \int_0^1 \left(\frac{\partial^2 \delta^*}{\partial x^{*2}}\right)^2 \mathrm{d}x^*,\tag{11}$$

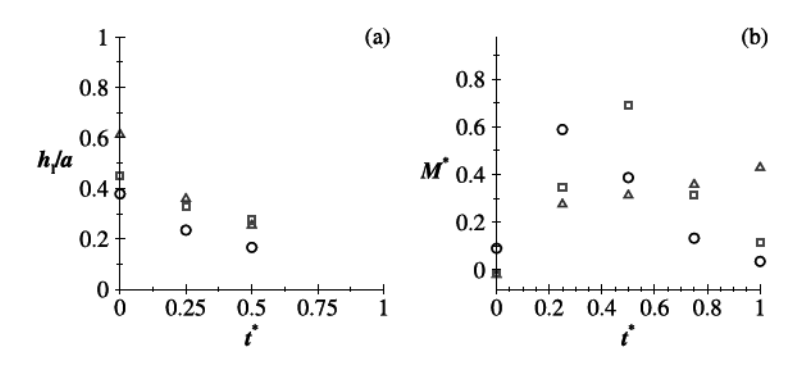


Fig. 10. a) Non-dimensional lower core separation distance from the plate surface, and b) non-dimensional applied moment at the plate base over the duration $0 \le t^* \le 1$ at $H_0^*/a^* = 1.37$ and $f^* = 1.0$, Δ represent St = 0.20 ($\Pi_m = 11.4$), \square represent St = 0.070 ($\Pi_m = 95.1$), and \square represent St = 0.040 ($\Pi_m = 251$).

$$E_{\mathbf{k}} = \frac{m_{\mathbf{s}}LWU^2}{2} \int_0^1 \left(\frac{\partial \delta^*}{\partial t^*}\right)^2 \mathrm{d}\mathbf{x}^*. \tag{12}$$

In Eqs. (11) and (12) it is assumed that the spatial distribution of the deflection is well approximated by the first mode of vibration [51] because only the tip deflection is known from the laser displacement sensor. The PIV recordings confirmed that the plate oscillations are prescribed well by the first mode.

The total plate energy is found as a summation of the spatially-averaged strain and kinetic energies, which gradually decays due to structural and fluid damping until the next vortex ring again adds energy to the system. Therefore, a temporally-averaged measure of the total energy can be computed by averaging over the non-dimensional vortex production period, $T_p^* = (f^*St)^{-1}$, such that

$$\overline{E_{t}} = \frac{1}{T_{p}^{*}} \int_{0}^{T_{p}^{*}} (E_{s} + E_{k}) dt^{*}.$$
(13)

The total energy can be non-dimensionalized by the kinetic energy available in each incoming vortex ring, $\overline{E_t^*} = \overline{E_t}/E_0$. Assuming the vortex ring has a thin core, the kinetic energy of a vortex ring, E_0 , can be approximated as [52]

$$E_0 = \frac{1}{4}\rho \Gamma^2 a [\ln(\frac{8a}{h}) - 2]. \tag{14}$$

This thin core assumption is admittedly strained in the present case, where b/a = 0.33-0.37; nevertheless, the value serves as a consistent reference by which relative magnitudes of energy can be compared. We note that the normalized total plate energy, $\overline{E_t}/E_0$, does not represent the amount of energy transferred to the plate by a given vortex ring.

The total non-dimensional energy as a function of the non-dimensional frequency ratio is shown in Fig. 11 on a logarithmic scale, at two different distance ratios of $H_0^*/a^* = 1.37$ and 1.91. The measurements of plate energies were repeated at $H_0^*/a^* = 1.91$ to provide a quantitative comparison on the effect of distance ratio, as well as the frequency ratio and plate mass parameter. The colored lines/symbols in each plot denote the influence of Strouhal number on the energy exchange by distinguishing the behavior as a function of the non-dimensional plate mass parameter.

The portion of the vortex ring nearest the plate is initially tangent to its surface at $H_0^*/a^* = 1.37$. If the distance from the center of the lower vortex ring core to the plate surface at rest is defined as h_{10} , its ratio to the core radius, h_{10}/b , is equal to 1 at $H_0^*/a^* = 1.37$. This value is equal to $h_{10}/b = 2.50$ for the case of $H_0^*/a^* = 1.91$. Comparing Fig. 11(a) with Fig. 11(b), it is then observed that increasing the vortex core-to-plate separation distance (h_{10}/b) by 2.5 times (i.e., the lower core is 2.5 times farther from the plate) results in a decrease in the plate energy by approximately an order of magnitude. Similar behavior has been reported for discrete vortex interactions, where the energy was shown to decrease exponentially as the distance ratio increased [34]. Excitation of the plate at resonance, as opposed to discrete loading, increases the non-dimensional plate energy by approximately 3 orders of magnitude. This demonstrates that even at sub-optimal conditions, where vortex rings are advecting tangentially over one side of a plate, a considerable amount of energy can be captured from the vortices if the natural frequency of the plate is matched with the vortex production frequency. Furthermore, it can be observed that driving the plate

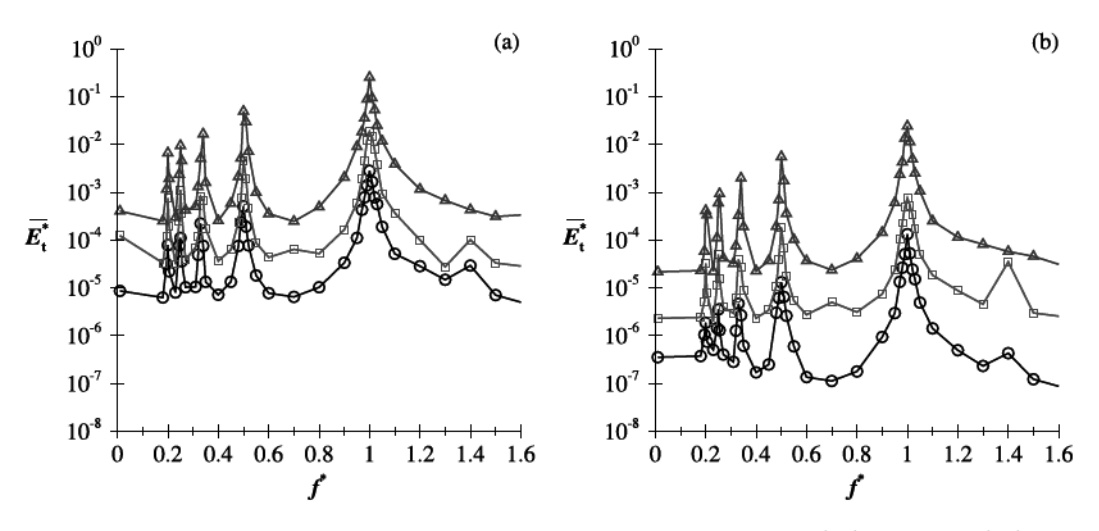


Fig. 11. Total spatially- and temporally-averaged non-dimensional plate energy over one period of vortex production at a) $H_0^*/a^* = 1.37$, and b) $H_0^*/a^* = 1.91$. \triangle represent St = 0.20 ($\Pi_m = 11.4$), \square represent St = 0.070 ($\Pi_m = 95.1$), and \bigcirc represent St = 0.040 ($\Pi_m = 251$).

at sub-harmonic frequencies will also increase the absorbed energy significantly; by approximately 2 orders of magnitude in comparison with the discrete loading scenario.

As the Strouhal number increases (decreasing Π_m), the plate energy increases. Increasing the Strouhal number by almost an order of magnitude (St = 0.040 to St = 0.20) increases the plate energy at resonance by approximately two orders of magnitude. Hu et al. [24] found that for inviscid interactions, St \sim 0.5 maximizes the vortex-plate energy exchange for a discrete vortex pair advecting tangentially over the plate surface. This value corresponds to the time for the vortex to propagate over the plate being equal to exactly one half of the plate oscillation period, with the loading timed such that it is in phase with the plate trajectory. This value of optimal Strouhal number is, however, expected to be influenced by the presence of fluid viscosity, as vortex-plate vorticity interactions will be influenced by flow separation along the plate, cross-sign vorticity annihilation, vortex break down, etc. For the current investigations, St \ll 0.5, and as such, the loading produces suboptimal energy transfer, and behaves largely as an impulse. Nevertheless, changes in the plate energy as a function of Strouhal number are clearly evident, with increased Strouhal numbers corresponding with increased plate energy. Future investigations are planned to more fully-investigate the dependence of vortex-plate energy exchange on Strouhal number in viscous flows, with an emphasis on identifying optimal conditions.

In energy harvesting applications, the conversion efficiency of mechanical strain energy into an output electrical energy by electro-active polymers depends strongly on the electro-mechanical coupling factor, excitation frequency, mechanical damping, and electrical load [53]. For the plate with St = 0.20 ($\Pi_{\rm m}=11.4$), which displays the highest plate energy in Fig. 11, the temporally-averaged strain energy at resonance at $H_0^*/a^*=1.37$ is equal to $\overline{E_{\rm s}}=11.6\,\mu{\rm J}$. Assuming a conversion efficiency of $\eta=10\%$, the output electrical energy can be estimated as $\overline{E_{\rm e}}=1.16\,\mu{\rm J}$. This produces a time-averaged electrical power output of $\overline{P_{\rm e}}=\eta d\overline{E_{\rm s}}/dt=25.5\,\mu{\rm W}$, which is comparable to previously reported values attainable with piezoelectric energy harvesters [54,55]. The power output could be further increased by lowering the mass parameter while maintaining the stiffness parameter constant (see Fig. 2), however, this was unfortunately not achievable in the current work due to experimental limitations. Note that the highest value of the mass parameter that was investigated ($\Pi_{\rm m}=251$) (see Fig. 2) is outside the range of normal energy harvesting applications, as it was designed for the investigation of voiced speech, as will subsequently be discussed.

4.4. Application to voiced speech

As previously discussed, the structural properties of the vocal folds can be modeled as a plate with parameters $\Pi_{\rm m}=251$ and $\Pi_{\rm s}=1.51$. It should be noted, however, that modeling the vocal fold structure as a plate is a first-order approximation. The boundary conditions and vocal fold geometry are greatly simplified, and consequently, do not capture the higher order oscillation modes of the vocal fold structure [56]. In addition, tissue damping is neglected. Vortex roll-up/formation within the glottis is also not considered in this study. Nevertheless, these simplifications are likely to result in an over-estimation of the influence of vortex loading on the vocal fold structure, because the fixed-free boundary condition of the current model results in higher deflection amplitudes than the fixed-fixed boundary condition of the actual vocal folds. Consequently, the current formulation provides an upper limit for determining the influence of intra-glottal vortices on the vocal fold dynamics. By decoupling the vortex loading from the bulk aerodynamic loading that occurs in voiced speech, it is possible to infer the impact of intra-glottal vortices on the vocal fold dynamics.

The chosen physical plate dimensions correspond to 50 times life-size, and the properties of the plate and the vortices, when scaled to life-size, are listed in Table 4 along with the normal range of physiological values. The plate parameters are good representations of the physiological properties of voiced speech. Note the experimental limitations prevented matching the Reynolds numbers of the flow. However, any variations in loading as a function of Reynolds number can be deemed negligible as both the experimental and life-size scenarios produce laminar vortex rings.

The fundamental frequency of the model is within the the range of typical values, reported to be around 80–220 Hz [29]. The value of the modulus of elasticity in Table 4 shows that the current model is close to the upper limit of the range reported by Alipour and Vigmostad [44]. It was not possible to achieve a model with a lower modulus of elasticity due to experimental limitations. However, the current model provides a reasonable estimate for determining the impact of intra-glottal vortices on the vocal fold dynamics.

Table 4Properties of the cantilevered plate model of voiced-speech. The reported values are scaled to life-size, and corresponding physiological measures are reported.

. 0.7	•			
Description	Variable	Scaled Value	Physiological Values	[Units]
Length	L	1.7	1.0-3.0	[mm]
Width	W	15	12-17	[mm]
Thickness	T	0.50	0.50-1.0	[mm]
Modulus of elasticity	E	19.9	1.00-20.0	[Kpa]
Fundamental frequency	f_{o}	130	80-220	[Hz]
Advection velocity	U	5.00	5.00-15.0	[m/s]

The procedure outlined by Hu et al. [24] is used in this study to convert the two-dimensional line vortices produced during voiced speech to equivalent three-dimensional vortex rings and obtain the equivalent circulation and distance ratios that produce a comparable pressure loading. Based on experimental PIV data [27], the non-dimensional circulation of a vortex ring that is representative of the loading produced by an intra-glottal line vortex was computed to be $\Gamma^*=0.90$. The experimental PIV data were also used to determine the average equivalent distance ratio between the vortices and the vocal fold surfaces as approximately $H^*/a^*=1.80$. In the current study, the highest loading case is considered, where the distance ratio is $H_0^*/a^*=1.37$. As such, the previously introduced case of $\Pi_{\rm m}=251$, and $f^*=1.0$ at $H_0^*/a^*=1.37$ is an appropriate model of vortex-induced vibrations in the vocal fold structure.

As observed in Fig. 11(a), the plate representative of the vocal folds ($\Pi_{\rm m}=251$) gains a very small amount of energy from the vortex rings when excited at resonance conditions and a distance ratio of $H_0^*/a^*=1.37$. At resonance, the total plate energy, imparted from the steady-state periodic passage of many vortex rings, is only 1.1% of the energy of an *individual* vortex ring. Grossly assuming that this value of 1.1% is the energy transferred to the plate by each successive ring (a very large overestimation), this value can be compared to the total aerodynamic energy transfer that occurs during one cycle of the vocal fold oscillations to estimate the portion of the total fluid loading that arises due to intra-glottal vortices. Prior work utilized numerical simulations to calculate the total aerodynamic energy transferred to the vocal folds over one phonatory cycle [57]. It was reported that the energy per unit width imparted to the vocal folds during the open phase of vocal fold oscillation was $\overline{E}_T/W=1.37$ J/m. Scaling the energy transferred to the plate at $H_0^*/a^*=1.37$ and $f^*=1.0$ to the corresponding life-size value according to the parameters listed in Table 4 reveals that the maximum energy transfer per unit width attainable for periodic vortices advecting over the vocal fold surface at resonance conditions will be $\overline{E}_t/W<2.98\times10^{-4}$ J/m. Thus the ratio of energy transfer due to vortex loading to total aerodynamic energy transfer is $\overline{E}_t/\overline{E}_T<2.0\times10^{-2}\%$, demonstrating, as others have suggested [32,33], that intra-glottal vortices will have a negligible influence on the pressure loading experienced by the vocal folds during normal voiced speech production. However, it should be emphasized that intra-glottal vortices can be a key acoustic sound source in voiced speech production [29].

5. Conclusion

The interactions of discrete and periodic vortex rings advecting tangentially over the surface of cantilevered plates were investigated with application to energy harvesting and voiced speech production. Three polycarbonate plates were manufactured with the same non-dimensional stiffness parameter and varying non-dimensional mass parameters. The displacement time history, vorticity field, pressure field, and energy transfer were reported as a function of the vortex production frequency.

The variation of plate tip deflection amplitude with respect to frequency ratio revealed that a two order of magnitude increase is observed when the plate is driven at resonance as opposed to by a discrete vortex ring. It was also shown that excitation of the plate at sub-harmonics (integer fractions of the plate fundamental frequency) will increase the plate deflection amplitude by approximately an order of magnitude over the discrete loading scenario.

The plate dynamics were characterized by two stages of energy transfer: (1) pressure loading along the plate arising from the core of a coherent vortex; and (2) pressure loading along the plate as cross-sign interactions between the plate and vortex ring vorticity led to vortex break down. Higher initial plate tip deflections arising from increased oscillation amplitudes increased the instantaneous vortex-to-plate distance ratio, delaying cross-sign vorticity interactions, and causing a temporal shift in the location of the peak moment applied by the vortex ring.

Variation of non-dimensional plate energy as a function of the frequency ratio resulted in an increase of approximately three orders of magnitude when the plate was excited at resonance, and about two orders of magnitude increase when the plate was excited at sub-harmonics, when compared to excitation by a discrete vortex ring. It was also shown that the total amount of plate energy arising from the periodic vortex loadings was dependent upon the Strouhal number, with higher values producing higher plate energy despite having similar spatially-averaged pressure loads.

Lastly, a model of vortex-structure energy exchange during voiced speech production was considered, employing a plate that was representative of the structural properties of the vocal folds. Determination of the energy exchange between the vortices and the plate at resonance conditions showed that vortices are only responsible for a vanishingly small fraction of the total aerodynamic energy transfer that occurs during normal voiced speech production.

Acknowledgements

This material is based upon work supported by the National Science Foundation (NSF) under Grant No. CBET-1511761, and the Natural Sciences and Engineering Research Council of Canada (NSERC), under Grant No. 05778-2015.

References

- [1] D. Rockwell, Vortex-body interactions, Annu. Rev. Fluid Mech. 30 (1998) 199-229, https://doi.org/10.1146/annurev.fluid.30.1.199.
- [2] C.H.K. Williamson, R. Govardhan, A brief review of recent results in vortex-induced vibrations, J. Wind Eng. Ind. Aerod. 96 (2008) 713–735, https://doi.org/ 10.1016/j.jweia.2007.06.019.
- [3] R. Parameshwarana, S.J. Dhulipallaa, D.R. Yendluri, Fluid-structure interactions and flow induced vibrations: a review, Process Eng. 144 (2016) 1286–1293, https://doi.org/10.1016/j.proeng.2016.05.124.

- [4] A.B. Rostami, M. Armandei, Renewable energy harvesting by vortex-induced motions: review and benchmarking of technologies, Renew. Sustain. Energy Rev. 70 (2017) 193–214, https://doi.org/10.1016/j.rser.2016.11.202.
- [5] A. Abdelkefi, Aeroelastic energy harvesting: a review, Int. J. Eng. Sci. 100 (2016) 112-135, https://doi.org/10.1016/j.ijengsci.2015.10.006.
- [6] M.J. Shelley, J. Zhang, Flapping and bending bodies interacting with fluid flows, Annu. Rev. Fluid Mech. 43 (2011) 449–465, https://doi.org/10.1146/annurev-fluid-121108-145456.
- [7] M.Q. Le, J.F. Capsal, M. Lallart, Y. Hebrard, A. Van Der Ham, N. Reffe, L. Geynet, P.J. Cottinet, Review on energy harvesting for structural health monitoring in aeronautical applications, Prog. Aero. Sci. 3 (2015) 052004, https://doi.org/10.1016/j.paerosci.2015.10.001.
- [8] R. Murray, J. Rastegar, Novel twostage Piezoelectricbased ocean wave energy harvesters for moored or unmoored buoys, Act. Passiv. Smart Struct. Integr. Syst. 7288 (2009) 72880E, https://doi.org/10.1117/12.815852.
- [9] H.D. Akaydin, N. Elvin, Y. Andreopoulos, Energy harvesting from highly unsteady fluid flows using piezoelectric materials, J. Intell. Mater. Syst. Struct. 21 (2010) 1263–1278, https://doi.org/10.1177/1045389X10366317.
- [10] Y. Cha, W. Chae, H. Kim, H. Walcott, S.D. Peterson, M. Porfiri, Energy harvesting from a piezoelectric biomimetic fish tail, Renew. Energy 86 (2015) 449–458, https://doi.org/10.1016/j.renene.2015.07.077.
- [11] L. Zuo, X. Tang, Large-scale vibration energy harvesting, J. Intell. Mater. Syst. Struct. 24 (2013) 1405–1430, https://doi.org/10.1177/1045389X13486707.
- [12] H. Li, C. Tian, J. Lu, M.J. Myjak, J.J. Martinez, R.S. Brown, Z. Daniel Deng, An energy harvesting underwater acoustic transmitter for aquatic animals, Sci. Rep. 6 (2016) 33804, https://doi.org/10.1038/srep33804.
- [13] G.W. Taylor, J.R. Burns, S.M. Kammann, W.B. Powers, W.T.R, The Energy Harvesting Eel: a small subsurface ocean/river power generator, IEEE J. Ocean. Eng. 26 (2001) 539–547, https://doi.org/10.1109/48.972090.
- [14] A. Giacomello, M. Porfiri, Underwater energy harvesting from a heavy flag hosting ionic polymer metal composites, J. Appl. Phys. 109 (2011) 084903, https://doi.org/10.1063/1.3569738.
- [15] H.D. Akaydin, N. Elvin, Y. Andreopoulos, The performance of a self-excited fluidic energy harvester, Smart Mater. Struct. 21 (2012) 025007, https://doi.org/10.1088/0964-1726/21/2/025007.
- [16] L.A. Weinstein, M.R. Cacan, P.M. So, P.K. Wright, Vortex shedding induced energy harvesting from piezoelectric materials in heating, ventilation and air conditioning flows. Smart Mater Struct. 21 (2012) 045002. https://doi.org/10.1009/0964.1726/21/4/045002
- conditioning flows, Smart Mater. Struct. 21 (2012) 045003, https://doi.org/10.1088/0964-1726/21/4/045003.
 [17] G. Yao, H. Wang, C. Yang, Research and design of underwater flow-induced vibration energy harvester based on Karman vortex street, Mod. Phys. Lett. B 31 (2017) 1750076, https://doi.org/10.1142/S0217984917500762.
- [18] H.D. Akaydin, N. Elvin, Y. Andreopoulos, Wake of a cylinder: a paradigm for energy harvesting with piezoelectric materials, Exp. Fluid 49 (2010) 291–304, https://doi.org/10.1007/s00348-010-0871-7.
- [19] J. Allen, A. Smits, Energy harvesting eel, J. Fluid Struct. 15 (2001) 629–640, https://doi.org/10.1006/jfls.2000.0355.
- [20] S.D. Peterson, M. Porfiri, Energy exchange between a vortex ring and an ionic polymer metal composite, Appl. Phys. Lett. 100 (2012) 114102, https://doi.org/10.1063/1.3693184.
- [21] E. Zivkov, S. Yarusevych, M. Porfiri, M.D. Peterson, Numerical investigation of the interaction of a vortex dipole with a deformable plate, J. Fluid Struct. 58 (2015) 203–215, https://doi.org/10.1016/j.jfluidstructs.2015.08.009.
- [22] E. Zivkov, S.D. Peterson, S. Yarusevych, Combined experimental and numerical investigation of a vortex dipole interaction with a deformable plate, J. Fluid Struct. 70 (2017) 201–213, https://doi.org/10.1016/j.jfluidstructs.2017.01.012.
- [23] O. Goushcha, N. Elvin, Y. Andreopoulos, Interactions of vortices with a flexible beam with applications in fluidic energy harvesting, Appl. Phys. Lett. 104 (2014) 2, https://doi.org/10.1063/1.4861927, ISSN 00036951.
- [24] J. Hu, M. Porfiri, S.D. Peterson, Energy transfer between a passing vortex ring and a flexible plate in an ideal quiescent fluid, J. Appl. Phys. 118 (2015) 114902, https://doi.org/10.1063/1.4930804.ISSN 0021-8979.
- [25] S.D. Peterson, M. Porfiri, Interaction of a vortex pair with a flexible plate in an ideal quiescent fluid, J. Intell. Mater. Syst. Struct. 23 (2012) 1485–1504, https://doi.org/10.1177/1045389X11435995, ISSN 1045-389X.
- [26] B.D. Erath, M.W. Plesniak, An investigation of bimodal jet trajectory in flow through scaled models of the human vocal tract, Exp. Fluid 40 (2006) 683–696, https://doi.org/10.1007/s00348-006-0106-0.
- [27] B.D. Erath, M.W. Plesniak, Viscous flow features in scaled-up physical models of normal and pathological vocal phonation, Int. J. Heat Fluid Flow 31 (2010) 468–481, https://doi.org/10.1016/j.ijheatfluidflow.2010.02.014.
- [28] S. Khosla, S. Murugappan, E. Gutmark, R. Scherer, Vortical flow field during phonation in an excised canine larynx model, Ann. Otol. Rhinol. Laryngol. 116 (2007) 217–228, https://doi.org/10.1177/000348940711600310.
- [29] R. Mittal, B.D. Erath, M.W. Plesniak, Fluid dynamics of human phonation and speech, Annu. Rev. Fluid Mech. 45 (2013) 437–467, https://doi.org/10.1146/annurev_fluid-011212-140636.
- aminute-inductifize induction and induction and induction in the induction
- [31] L. Oren, S. Khosla, E. Gutmark, Intraglottal pressure distribution computed from empirical velocity data in canine larynx, J. Biomech. 47 (2014) 1287–1293, https://doi.org/10.1016/j.jbiomech.2014.02.023.
- [32] M.H. Farahani, Z. Zhang, A computational study of the effect of intraglottal vortex-induced negative pressure on vocal fold vibration, J. Acoust. Soc. Am. 136 (2014) 5, https://doi.org/10.1121/1.4898743.
- [33] B. Kettlewell, S.D. Peterson, Ascertaining the Influence of Intraglottal Vortices upon the Dynamics of the Vocal Folds, Canadian Congress of Applied Mechanics, London, Ontario, Canada, 2015.
- [34] A. Pirnia, J. Hu, S.D. Peterson, B.D. Erath, Vortex dynamics and flow-induced vibrations arising from a vortex ring passing tangentially over a flexible plate, J. Appl. Phys. 122 (2017) 164901, https://doi.org/10.1063/1.5009068.
- [35] E.H. Mansfield, The Bending and Stretching of Plates, second ed., Cambridge University Press, Cambridge, U.K., 1989.
- [36] J.D. Hobeck, D.J. Inman, A distributed parameter electromechanical and statistical model for energy harvesting from turbulence-induced vibration, Smart Mater. Struct. 23 (2014) 115003, https://doi.org/10.1088/0964-1726/23/11/115003.
- [37] J. Wang, A. McDaid, R. Sharma, K.C. Aw, A compact ionic polymer metal composite (IPMC) system with inductive sensor for closed loop feedback, Actuators 4 (2015) 114–126, https://doi.org/10.3390/act4020114.
- [38] S. Orregó, K. Shoele, A. Ruas, K. Doran, B. Caggiano, R. Mittal, S.H. Kang, Harvesting ambient wind energy with an inverted piezoelectric flag, Appl. Energy 194 (2017) 212–222, https://doi.org/10.1016/j.apenergy.2017.03.016.
- [39] X. Gao, W.H. Shih, W.Y. Shih, Flow energy harvesting using piezoelectric cantilevers with cylindrical extension, IEEE Trans. Ind. Electron. 60 (2013) 1116–1118, https://doi.org/10.1109/TIE.2012.2187413.
- [40] M. Hirano, Phonosurgery: basic and clinical investigations, Otologia 21 (1975) 239–240.
- [41] J.E. Kelleher, T. Siegmund, R.W. Chan, E.A. Henslee, Optical measurements of vocal fold tensile properties: implications for phonatory mechanics, J. Biomech. 44 (2011) 1729–1734, https://doi.org/10.1016/j.jbiomech.2011.03.037.
- [42] I.R. Titze, Principles of Voice Production, Prentice Hall, New Jersey, U.S., 1994.
- [43] B.H. Story, T. I. R, Voice simulation with a body-cover model of the vocal folds, J. Acoust. Soc. Am. 97 (1994) 1249-1260, https://doi.org/10.1121/1.412234.
- [44] F. Alipour, S. Vigmostad, Measurement of vocal folds elastic properties for continuum modeling, J. Voice 26, https://doi.org/10.1016/j.jvoice.2012.04.010.
- [45] M. Gharib, E. Rambod, K. Shariff, A universal time scale for vortex ring formation, J. Fluid Mech. 360 (1998) 121–140, https://doi.org/10.1017/ S0022112097008410, ISSN 00221120.
- [46] P. Kabiri, Active Flow Control over a NACA 0015 Airfoil by Synthetic Jet Actuators, Ph.D. thesis, Clarkson University, 2012.
- [47] A. Glezer, The formation of vortex rings, Phys. Fluids 31 (1988) 3532, https://doi.org/10.1063/1.866920.
- [48] A. Shams, M. Jalalisendi, M. Porfiri, Experiments on the water entry of asymmetric wedges using particle image velocimetry, Phys. Fluids 27 (2015) 2, https://doi.org/10.1063/1.4907745.

- [49] Y.H. Tseng, F. J. H, A ghost-cell immersed boundary method for flow in complex geometry, J. Comput. Phys. 192 (2003) 593–623, https://doi.org/10.1016/j.icp.2003.07.024.
- jcp.2003.07.024.
 [50] T.T. Lim, A note on the leapfrogging between two coaxial vortex rings at low Reynolds numbers, Phys. Fluids 9 (1998) 239, https://doi.org/10.1063/1.869160.
- [51] D.J. Inman, Engineering Vibration, Pearson Education, New Jersey, U.S., 2014.
- [52] P.H. Roberts, R.J. Donnelly, Dynamics of vortex rings, Phys. Lett. 31 (1970) 137-138, https://doi.org/10.1016/0375-9601(70)90193-3.
- [53] Z. Yang, A. Erturk, J. Zua, On the efficiency of piezoelectric energy harvesters, Extreme Mech. Lett. 15 (2017) 26–37, https://doi.org/10.1016/j.eml.2017.05.
- [54] Q. Wang, N. Wu, Optimal design of a piezoelectric coupled beam for power harvesting, Smart Mater. Struct. 21 (2012) 085013, https://doi.org/10.1088/0964-1726/21/8/085013.
- [55] M.W. Shafer, M. Bryant, E. Garcia, Erratum: designing maximum power output into piezoelectric energy harvesters, Smart Mater. Struct. 21 (2012) 109601, https://doi.org/10.1016/j.eml.2017.05.002.
- [56] D.A. Berry, I.R. Titze, Normal modes in a continuum model of vocal fold tissues, J. Acoust. Soc. Am. 100 (1996) 3345, https://doi.org/10.1121/1.416975.
- [57] S.L. Thomson, L. Mongeau, S.H. Frankel, Aerodynamic transfer of energy to the vocal folds, J. Acoust. Soc. Am. 118 (2005) 1689, https://doi.org/10.1121/1. 2000787.